Friction **11**(6): 1040–1056 (2023)
https://doi.org/10.1007/s40544-022-0646-1
ISSN 2223-7690
CN 10-1237/TH
RESEARCH ARTICLE

Electron transfer dominated triboelectrification at the hydrophobic/slippery substrate–water interfaces

Yi CHEN[1,3], Xiaojuan LI[1,3], Chenggong XU[1,3], Daoai WANG[1], Jinxia HUANG[1,3,*], Zhiguang GUO[1,2,*], Weimin LIU[1,3,*]

[1] *State Key Laboratory of Solid Lubrication, Lanzhou Institute of Chemical Physics, Chinese Academy of Sciences, Lanzhou 730000, China*

[2] *Ministry of Education Key Laboratory for the Green Preparation and Application of Functional Materials, Hubei University, Wuhan 430062, China*

[3] *University of Chinese Academy of Sciences, Beijing 100049, China*

Received: 20 January 2022 / Revised: 15 March 2022 / Accepted: 04 May 2022

Abstract: Triboelectric nanogenerator (TENG) based on triboelectrification has attracted wide attention due to its effective utilization of green energy sources such as marine energy. However, researches about liquid–liquid triboelectrification are still scanty as solid–liquid triboelectrification has been widely studied. Herein, this work focuses on the hydrophobic/slippery substrate–water interfacial triboelectrification based on the solid friction materials of polytetrafluoroethylene (PTFE) nanoparticles. The hydrophobic/slippery substrate–water interfacial triboelectrification are studied by assembling PTFE coated Al sheets and perfluoropolyether (PFPE) infused PTFE coated Al sheets (formed the slippery lubricant-infused surfaces (SLIPSs)) as the friction electrode, and water as liquid friction materials, respectively. The results show that the hydrophobic TENG output performances improved as the PTFE nanoparticles cumulating, and the SLIPSs TENG output performances increased with the thinner PFPE thickness. Both the triboelectrification behavior of hydrophobic/SLIPSs TENG assembled in this work are dominated by the electron transfer. Thanks to the introduction of SLIPSs, the SLIPSs TENG exhibits superior stability and durability than the hydrophobic TENG. The investigation of hydrophobic/slippery substrate–water interfacial triboelectrification contributes to optimize the TENG performances, and expands the application in harsh environments including low temperature and high humidity on the ocean.

Keywords: triboelectric nanogenerator (TENG); slippery lubricant-infused surfaces (SLIPSs); polytetrafluoroethylene (PTFE) nanoparticles; perfluoropolyether (PFPE)

1 Introduction

With the worsening of the global climate changes, there are huge carbon emission derived from the use of petroleum, coal, and other. For achieving the goals of CO_2 emissions peak and carbon neutrality, new green energy is urgently need to be developed [1, 2]. The ocean energy has received increasing attention as one of the renewable energies [3–6]. Waves are a form of ocean energy source that is often considered hazardous to transportation, but can be extremely powerful if harnessed properly. The triboelectrification is a universal phenomenon happens everywhere, and the triboelectric nanogenerator (TENG) is developed based on the triboelectrification [7–10]. The contact–separation mode, one of many forms of TENG, can convert mechanical energy into electrical energy, and is one of the effective ways to utilize the wave energy [11, 12]. Moreover, the triboelectrification characteristics of contact–separation mode TENG are needed to be

* Corresponding authors: Jinxia HUANG, E-mail: huangjx@licp.cas.cn; Zhiguang GUO, E-mail: zguo@licp.cas.cn; Weimin LIU, E-mail: wmliu@licp.cas.cn

researched for different types of interfaces. In addition to the common solid–solid contact, solid–liquid, liquid–liquid interfacial contact also allured increasing attentions thanks to its potential applications in wave energy collection [12–16].

In the triboelectrification of the solid–liquid interfaces, the two-step formation process of the electric double layer (EDL) is the generally accepted theory, containing the contact electrification and electrostatic induction [17–21]. When liquid molecules contact with solid molecules, the electron clouds overlap and electrons are transferred from one phase to the other, which is called the contact electrification. Therein, due to the fluidity of liquid, the closer contact of friction materials occurred in the solid–liquid TENG, enables the easier the electron transfer. After the electron transition, a layer of electrostatic charge is formed on the interface, and an electrostatic field in the contact interface formed. The ions in the liquid move oriented under the electrostatic interaction, which is the electrostatic induction process. Although this theory successfully explains the triboelectrification behavior, it's still varying in different situations, which need to be analyzed on a case-by-case basis.

The triboelectrification behavior usually occurs at two surfaces with different charge affinity when rubbing or contacting, and the larger different charge affinity resulting in the higher triboelectric charge density. In the traditional triboelectrification on the solid–liquid interface, the solid surfaces are generally hydrophobic with correspond liquid, which is beneficial to the separation of solid and liquid [20]. The polytetrafluoroethylene (PTFE) is usually electronegative and hydrophobic because of the abundant F atoms with strong electronegative [22], and water is usually electropositive [23]. The PTFE and water are usually selected as the friction pairs for the TENG studies due to the larger different charge affinity and the lossless separation between PTFE and water [24–28]. And the PTFE nanoparticles are appropriate choice duo to the large specific surface area and free of the shape, size of the substrate. So far, the effect of PTFE dispersion concentration on TENG is still unknown. Beyond that, the trapped air layer on the hydrophobic surfaces can be destroyed when suffered extreme situations, causing water droplets adhere on the solid surfaces. The forming of water films prevents the effective separation of water from the solid surfaces and restrains the generation of frictional charges, furthers the TENG ineffective [29]. Moreover, inspired by the nepenthes, the slippery lubricant-infused porous surfaces (SLIPSs) have a stable solid–liquid interface through replacing the air layer of hydrophobic surfaces with the lubricant [30]. It not only possesses the advantages of superhydrophobic surfaces, such as surface hydrophobic [31], antifouling [32], antiadhesion [33], anti-ice and anti-fog [34], anticorrosion [35] and antibacterial [36], but also shows excellent stability and self-repairing function in harsh environment [30]. PFPE are common lubricant in the SLIPSs due to the advantages of less volatile, low surface energy, immiscible with most liquids, and especially the good chemical inertia [37]. Therefore, the application of PFPE infused SLIPSs in the TENG will offer a new approach to the design of new energy harvesting devices, and overcome the defect of traditional hydrophobic solid–liquid TENG failure in harsh environment.

Herein, this work focuses on the triboelectrification based on the hydrophobic/slippery substrate–water interfaces. Firstly, The PTFE nanoparticles were coated on Al sheets with different structures by a simple spin-coating method, and then infused the perfluoropolyether (PFPE) to obtain the SLIPSs. The surfaces with the different interfacial characteristics were assembled to hydrophobic TENG and SLIPSs TENG symmetrically. The effects of PTFE dispersion concentrations and substrate structure on the hydrophobic TENG were investigated, and the flat Al sheets coated with 60 wt% PTFE dispersion exhibited the optimum performances since the more PTFE nanoparticles on the surfaces can generate higher charge density. Furthermore, the effect of PFPE thickness on the SLIPSs TENG was studied, and the thinner PFPE was beneficial to the triboelectrification due to a higher contact probability between water and PTFE layer. The researches of ethylene glycol based TENG and the response to different ionic concentrations indicated that both the triboelectrification behaviors of hydrophobic/SLIPSs TENG assembled in this work were dominated by the electron transfer. Thanks to the excellent properties of SLIPSs, the stability and

durability of SLIPSs TENG were strengthened by a thin PFPE layer on the surfaces. The investigation of hydrophobic/slippery substrate–water interfacial triboelectrification is contribute to optimize the TENG performances. Furthermore, the introduction of SLIPSs enhanced the stability and durability of TENG, expanding its application in harsh environments including low temperature and high humidity on the ocean.

2 Experimental

2.1 Materials

Al sheets (purity 99.999%, thickness 0.3 mm) were purchased from Zhongnuo Advanced Material (Beijing) Technology Co., Ltd., Beijing, China. Sodium chloride (NaCl) was purchased from Tianjin Lianlong Bohua Pharmaceutical Chemical Co., Ltd., China. PTFE concentrated dispersion (60 wt%) was purchased from Macklin Biochemistry Co., Ltd., Shanghai, China. The DuPont Krytox PFPE (GPL-103) lubricant was supplied by Chemours Company. All of the chemical reagents were of analytical grade and used without further purification. Deionized (DI) water was produced using a ModuPure system and used in all experiments.

2.2 Fabrication of PTFE coated Al sheets

This work focuses on the hydrophobic/slippery substrate–water interfacial triboelectrification based on the solid friction materials of PTFE nanoparticles. Therein, the PTFE nanoparticles were coated on the original Al sheets and etched Al sheets, and then lubricant was infused to obtain the lubricant infused nano/micro–nano surfaces. Firstly, the high-purity Al sheets were used as substrates and annealed at 400 °C for 5 h in a muffle to relieve the stress. Then the annealed high-purity Al sheets were ultrasonic rinsed in ethyl alcohol, acetone, 0.1 M HCl, and DI water respectively for 15 min and air-dried. The cleaned original Al sheets were labeled as O-Al. Besides, the Al sheets with multi-facet surfaces were prepared by electrochemical etching, which were carried out at a constant voltage 15 V for 2 h in 0.17 M NaCl solution with an Al sheet as positive electrode and a platinum sheet as negative electrode. The etched Al sheets were then thoroughly rinsed by DI water and air-dried for further use. The Al sheets after being etched was labeled as E-Al.

Preparation of PTFE dispersion. Different concentrations of PTFE dispersions were prepared with concentrated dispersion as raw material. 10 wt%, 20 wt%, 30 wt%, and 45 wt% PTFE dispersion were obtained by adding 15, 6, 3, and 1 g DI water into 3 g 60 wt% PTFE concentrated dispersion with ultrasonic dispersion 10 min, respectively. And the 60 wt% PTFE dispersion was direct from the raw materials.

Preparation of PTFE coated Al sheets. The different concentrations of PTFE dispersions were coated on O-Al and E-Al by a spin-coating instrument (VTC-100, MTI Corporation). 200 μL different concentrations of PTFE dispersions (10 wt%, 20 wt%, 30 wt%, 45 wt%, and 60 wt%) were coated on O-Al and E-Al at the first spin rate of 500 rpm for 10 s to make sure it evenly distributed on the surface and then at the second spin rate of 3,000 rpm for 60 s to remove the redundant dispersion. The Al sheets with PTFE dispersion coated were then heated to 300 °C for 2 h to remove the surfactant in the PTFE concentrated dispersion for higher hydrophobic. The different concentrations of PTFE dispersions coated O-Al and E-Al were marked as OP-x and EP-x (x represents different concentrations of PTFE dispersions and x = 10 wt%, 20 wt%, 30 wt%, 45 wt%, 60 wt%), respectively. Then 30 μL PFPE was uniformly coated on the surface of OP-x and EP-x, and were marked as FOP-x and FEP-x, respectively. The samples of FOP-x and FEP-x undergoing different spin rate were marked as y-FOP-x and y-FEP-x (y represents different spin rate and y = 1,000, 2,000, 3,000, 4,000, 5,000, 6,000, 7,000, 8,000 rpm), respectively.

Assembly of the TENG devices. The vibrative contact–separation mode TENG was employed in this work other than the droplets-based contact–separation mode TENG on account of the lubricant depletion of the SLIPSs after undergo drop impact [38, 39]. The hydrophobic TENG devices were assembled by OP-x and EP-x as the solid friction material, 5 mL water as the liquid friction material, and a highly transparent polycarbonate tube (PC tube with the outer diameter of 2 cm, the inner diameter of 1.8 cm, and the length

of 6 cm) as the container to carry the liquid (without other explanation, the liquid friction material was water). The hot melt adhesive was employed to assemble the solid friction materials and PC tube, and the liquid friction material was injected in the PC tube. Then two Cu wires were attached on the solid friction materials by Cu type. The SLIPSs TENG devices were assembled in the same way as the hydrophobic TENG devices except the solid friction materials OP-x and EP-x were replaced by the SLIPSs samples of y-FOP-x and y-FEP-x.

2.3 Characterizations

The microstructures of OP-x and EP-x were observed by a field-emission scanning electron microscopy (FESEM, QUANTA FEG 650, FEI, USA). The three-dimensional (3D) surface profiles and roughness of different states Al sheets, and the thickness of PTFE on O-Al surface were analyzed by a non-contact 3D surface profilometer (MicroXAM-800, KLA-Tencor, USA). The surface chemical components of different states Al sheets were investigated by a Fourier transform infrared spectrometer (FTIR, V70, Brooker, Germany) and X-ray photoelectron spectrometer (XPS, ESCALAB 250Xi, ThermoFisher Scientific, USA). The static contact angle (CA) and sliding angle (SA) of 10 μL water on different states Al sheets were measured by a JC2000D system (Zhongchen Digital Equipment Co., Ltd., Shanghai, China). The shear stability properties were tested by placing the samples on the spin-coating instrument and spinning at a speed of 1,000–8,000 rpm for 10 s. The mass loss, the CAs, and SAs were recorded to analyze the shear stability of SLIPSs. The PFPE thickness of y-FOP-60 was obtained by analyzing the reserved mass after undergoing different spin rate (the density of PFPE is 1.85 g/mL at 20 °C). The hydrophobic TENG system was assembled by OP-x and EP-x as the solid friction material, deionized water as liquid friction material, and a PC tube as the container. The included area of solid friction material by PC tube is 10.2 cm^2. Then two Cu wires were attached on the Al sheets by Cu type. The mechanical energy input of the TENG assembled in this work was carried out by using a linear motor with amplitude of 0.9 cm and frequency of 2 Hz to realize the horizontal vibration. This kind of vibration ensures the maximum contact and separation of the friction pairs. The SLIPSs TENG system was assembled by FOP-x and FEP-x as the SLIPSs and the same conditions with the hydrophobic TENG. The short-circuit current (I_{sc}) and the output voltage (V_{oc}) of the TENG system were collected by using an SR570 low-noise current amplifier (Stanford Research System) and NI-PCI6259 (National Instruments), respectively. The output signals of some TENG were noisy, which was processed by smoothing and shown in this work.

3 Results and discussion

Firstly, the samples OP-x and EP-x were fabricated by simply coating different concentrations of PTFE dispersions on O-Al and E-Al surfaces using a spin-coating instrument and followed a heating process. The SLIPSs samples were obtained by dropping the PFPE on the OP-x and EP-x. Figure 1(a) shows the surface morphology diagrams of OP-x and EP-x before and after PFPE coated, and the typical contact–separation model hydrophobic/SLIPSs TENG devices diagram. The PTFE nanoparticles were selected as the solid friction materials due to the high electronegativity [15], high specific surface area and free of the shape, size of the substrate, and water was selected as liquid friction material due to be electropositive easily [11, 40]. And the greatly difference charge affinity of PTFE nanoparticles and water made the higher friction charge density. Due to the discreteness of the PTFE nanoparticles, O-Al and E-Al were selected as the attached substrates. The surface roughness of O-Al and E-Al with different concentrations of PTFE dispersions coated was shown in Fig. 1(b). The roughness of PTFE dispersions coated O-Al was increasing as the thicker PTFE dispersions. The roughness of OP-45 and OP-60 was increasing remarkable mainly due to the uneven distribution of PTFE nanoparticles on O-Al surface caused by the difference of centrifugal force at different positions, and the higher the PTFE dispersion concentrations, the more obvious the difference. Due to the step-like microstructure of E-Al (Fig. S1(b) in the Electronic Supplementary Material (ESM)), PTFE nanoparticles were mainly filled in the large pores during spin coating (Figs. 1(d1)–1(d5)), the effect of

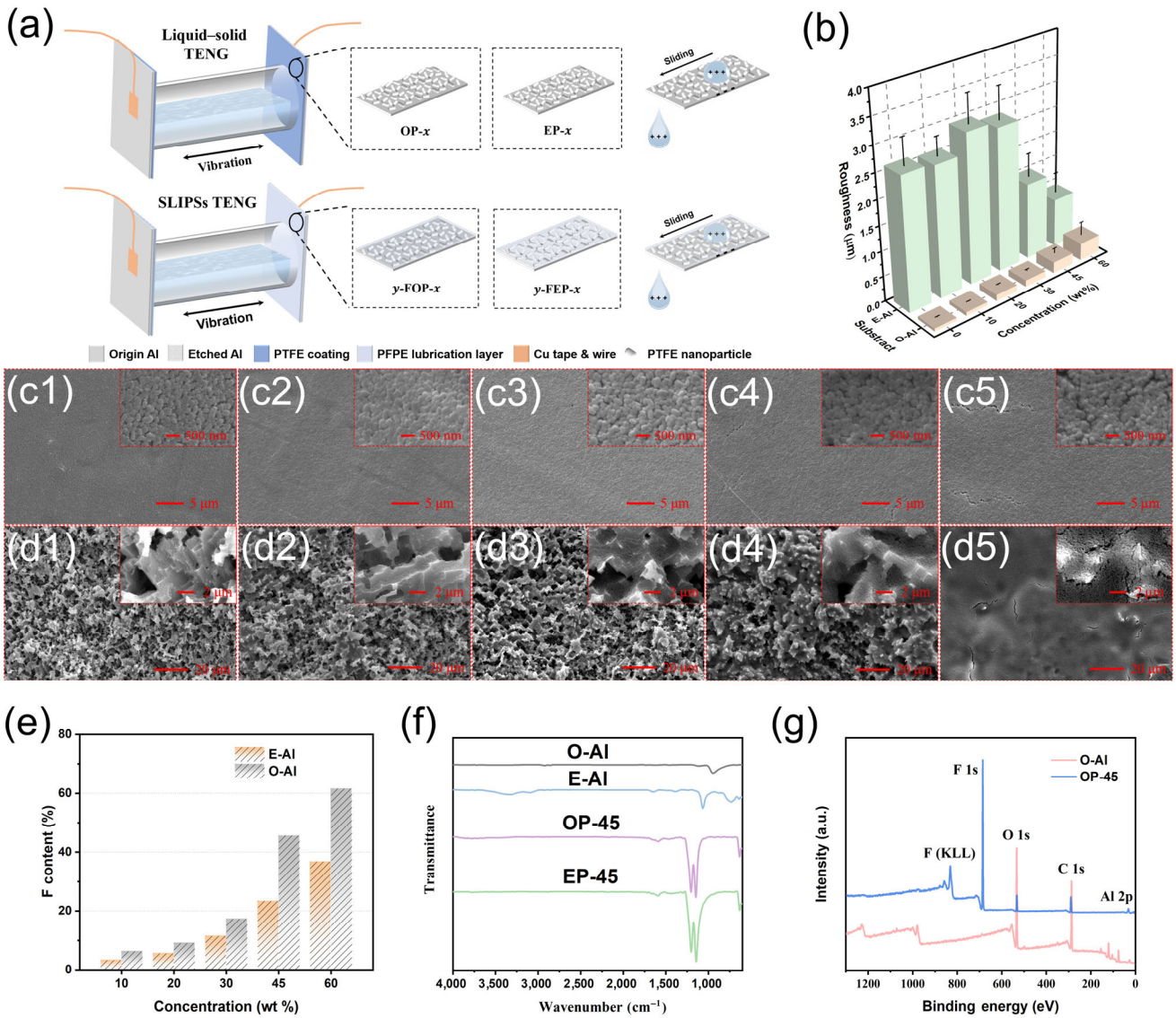

Fig. 1 Schematic of the TENG, the surface structure, and chemical constituents of different concentrations of PTFE dispersions coated O-Al and E-Al. (a) Schematic of the hydrophobic/SLIPSs TENG and the schematic of the morphology of different states Al sheets. (b) Roughness of OP-*x* and EP-*x*. (c1–c5) Nanostructure of OP-*x*, insets were the magnifying nanostructure. (d1–d5) Micro/nanostructure of EP-*x*, insets were the magnifying micro/nanostructure. (e) Percentage of element F in the total surface element content. (f) FTIR spectrum of O-Al, E-Al, OP-45, and EP-45. (g) XPS survey spectrum of O-Al and OP-45.

centrifugal force difference on E-Al surface was basically negligible. Thus, the roughness difference of EP-*x* was mainly affected by the concentrations of PTFE dispersion. The roughness of EP-10 was similar with the E-Al, and showed the maximum at the concentrations of 20–30 wt%. As the concentration of PTFE dispersions continued increasing, the PTFE nanoparticles gradually filled the pores of the step-like microstructure, and the roughness was decreased. Due to the step-like microstructure of E-Al, the roughness of PTFE coated E-Al was much higher than that of O-Al generally. Figure S1 in the ESM showed the SEM of O-Al and E-Al surfaces. The morphology of O-Al was flat, and E-Al was a typical step-like microstructure. Figures 1(c1)–1(c5) and Figs. 1(d1)–1(d5) showed the morphology of 10 wt%, 20 wt%, 30 wt%, 45 wt%, and 60 wt% PTFE dispersions coated O-Al and E-Al, respectively. The PTFE nanoparticles were uniformly covered on the surfaces of O-Al and E-Al, and the coated PTFE

nanoparticles were increased with the concentrate of PTFE dispersions increasing. When 10 wt% PTFE dispersions coated on the Al sheets, the PTFE nanoparticles distributed sporadically in the pores of the step-like microstructure of E-Al in small quantities (Fig. 1(d1)), whereas covered the O-Al surface uniformly with only some little gaps exposed to air (Fig. 1(c1)). The discrete distribution of PTFE nanoparticles on the E-Al surfaces basically had not effect on the surface roughness, which was consistent with the roughness analysis results. With the concentrate of PTFE dispersions increasing, numerous PTFE nanoparticles overlapped on the whole O-Al surfaces forming a stable PTFE layer (Figs. 1(c2)–1(c5)). And the higher content of F on the O-Al surfaces as the concentrate of PTFE dispersions increasing, representing the thicker PTFE layer on the O-Al surfaces (Fig. 1(e)). To confirm this, the thickness of PTFE on the O-Al surfaces was studied by using the non-contact 3D surface profilometer. The PTFE coated O-Al surfaces were scratched by a needle tip, and the altitude of a perpendicular line of the scratches was measured to obtain the thickness of PTFE layer. Figures S2 and S3 in the ESM showed the 3D surface profile images, altitude curves, and the thickness of PTFE layer on the O-Al surfaces. And the thicker the PTFE dispersions, the thicker the PTFE layer on the O-Al surfaces, which was corresponding with the results obtained by the content of F. As the concentrate of PTFE dispersions increasing, more PTFE nanoparticles distributed in the pores of the step-like microstructure of E-Al, and gradually filled them (Figs. 1(d1)–1(d5)). When the concentrate of PTFE dispersions was 60 wt%, the PTFE nanoparticles filled well in the pores of the step-like microstructure of E-Al only with bits of bulges exposed to air (Fig. 1(d5)). Figure 1(e) showed the percentage of F in the total surface element content. The content of F on PTFE dispersions coated O-Al and E-Al surfaces was increasing as the PTFE dispersion thickness. It is easy to understand that as the increasing concentrate of PTFE dispersions coated on the Al sheets, the higher F content, and the more PTFE nanoparticles on the Al sheets.. Meanwhile, the content of F on the O-Al surfaces was larger than that on the E-Al surfaces, which illustrated the poor PTFE nanoparticles retention capacity of the step-like microstructure than that of the flat structure.

The chemical constituents of O-Al, E-Al, OP-45, and EP-45 were researched by the FTIR spectrum as shown in Fig. 1(f). The absorption peak of O-Al was probably attributed to the aluminum oxide. The blunt absorption peak of E-Al at 3,000–3,600 cm^{-1} was belonged to the stretching vibration of the hydroxyl group (–OH), and the absorption peaks of E-Al at 1,645 and 1,690 cm^{-1} were ascribed to the deformation vibration absorption of –OH, which mainly demonstrated the hydroxide of aluminum existed on the E-Al surface. The absorption peaks of OP-45 and EP-45 at 1,140 and 1,200 cm^{-1} were belong to the stretching vibration of $–CF_2$ group. The FTIR results illustrated the E-Al surfaces were constituted by the hydroxide of aluminum, and the PTFE nanoparticles were coated on the O-Al and E-Al surfaces successfully. The element compositions of O-Al and OP-45 were also studied by XPS (Fig. 1(g)). The elements Al, O, and C were observed in the survey spectrum of O-Al, and the F 1s and its auger peak appeared in the spectrum of OP-45 with higher peak intensity of F. The results demonstrated that the different concentrations of PTFE dispersion were successfully coated on O-Al and E-Al, and show different morphology.

The PTFE nanoparticles are usually hydrophobic due to the lower surface tension (18.5 mN/m), whereas the O-Al and E-Al are hydrophilic due to numerous hydroxyls on the surfaces. Thus, the wettability of the O-Al and E-Al coated with PTFE dispersions varies with the PTFE concentrations. The wettability of PTFE nanoparticles coated O-Al and E-Al was investigated as shown in Fig. 2(a). The water CAs of OP-x were no significant fluctuation as the concentrations increases and stabled around 125°, which was due to the complete hydrophobic layer composed by PTFE nanoparticles. And the water was in Cassie–Baxter state on the OP-x surface. The PTFE nanoparticles was covered on the O-Al surfaces uniformly at the lowest PTFE dispersion concentrations with only some little gaps exposed to air, and the PTFE nanoparticles were completely filled the gaps as the concentrations increasing to form a totally PTFE layer. In this work, the PTFE dispersion coated Al sheets were heated at 300 °C for 2 h to remove the surfactant in the PTFE concentrated dispersion for higher hydrophobic. To confirm this, the 60 wt% PTFE

dispersion coated Al sheets were heated at 120 and 300 °C for 2 h respectively, and the water CAs were measured as shown in Fig. S4 in the ESM. The water CA of sample treated at 300 °C was higher than that of the sample treated at 120 °C. The water CAs of EP-*x* were increased with the concentrations increasing from 10 to 45 wt%, and were a little bit decreased at the concentrations of 60 wt%. The water CAs of EP-10 and EP-20 were smaller than that of other EP-based samples due to the trace amounts of hydrophobic PTFE nanoparticles sporadically distributed in the pores of step-like structure which still with a large amount of hydroxyl groups exposed on the surfaces, and the droplet was in Wenzel state on it. Because of more and more hydrophobic PTFE nanoparticles gradually filled in the pores of the step-like microstructure of hydrophilic E-Al surfaces, the decreased roughness made the water convert to Cassie–Baxter state, and water CAs increased. The water CAs show the maximum at the concentrations of 45 wt%, which was attributed to the synergistic effect of the micro bulges and PTFE nanoparticles. On the surface of EP-45, abundant PTFE nanoparticles filled in the step-like microstructure only with some of hydrophilic

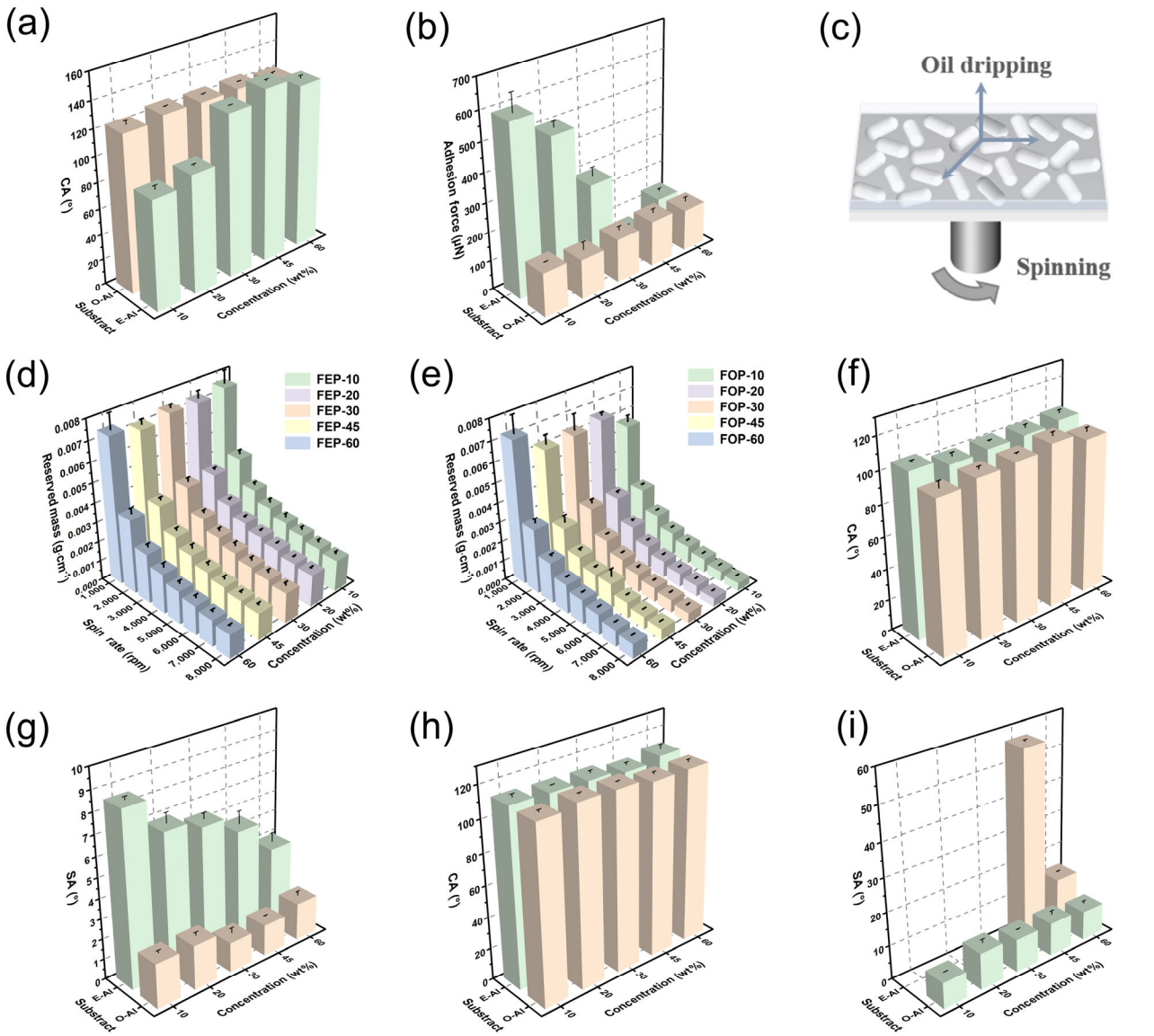

Fig. 2 Wettability and shear stability tests. (a) Water CAs of OP-*x* and EP-*x*. (b) Water adhesion force of OP-*x* and EP-*x*. (c) Diagram of the shear–spinning tests process. The reserved mass per unit area of lubricant of *y*-FOP-*x* (d) and *y*-FEP-*x* (e). Water CA (f) and SA (g) of FOP-*x* and FEP-*x*. Water CA (h) and SA (i) of 8000-FOP-*x* and 8000-FEP-*x*.

micro bulges exposed, which reduced the surface tension and roughness. But the water CA was decreased at the PTFE dispersion concentrations of 60 wt%, which was resulted from the lower roughness of EP-60 than other concentrations PTFE dispersion coated E-Al and the less micro bulges exposed. Meanwhile, the surfaces of EP-60 were basically flat due to the filling of PTFE nanoparticles, the water CAs of EP-60 was not much different from that of OP-60. In addition, the adhesion force of PTFE nanoparticles coated O-Al and E-Al was investigated as shown in Fig. 2(b). The adhesion force of OP-*x* was not fluctuated very much with the concentrations increases and stabled at around 145 μN, which was due to the complete hydrophobic layer composed by PTFE nanoparticles, and the water was in Cassie–Baxter state. Due to the discontinuity of the three-phase contact line under Cassie–Baxter state, the surfaces of OP-*x* have a small adhesion force, and water can roll easily on the solid surfaces. The adhesion force of EP-*x* was decreased with the concentrations increasing from 10 wt% to 45 wt% and increased at the concentrations of 60 wt%, which showed an opposite trend with the water CAs. The water was in Wenzel state on the surfaces of EP-10 and EP-20. The droplet in Wenzel state has a very large adhesion force on solid surfaces due to the expansion of three-phase contact line, and the droplet is easy to pin on the surfaces without falling off.

The rough micro/nanostructure is conducive to retain the lubricant under harsh conditions. The factors affecting the stability of the lubricating layer are the volatility and chemical inertia of the lubricating oil, and the strength of the bond with the substrates through capillarity and intermolecular force. The PFPE lubricant employed in this work has low steam pressure and excellent chemical inertia. Because the surface is coated by PTFE nanoparticles with small pores which help to improve the capillarity. The PTFE nanoparticles themselves are hydrophobic with low surface energy, and PFPE can easily wet the PTFE coated surface. Therefore, the strength of the bond with the substrates through capillarity and intermolecular force is sufficient to stabilize the lubricant layer. In addition, when suffering external forces, the lubricant layer was easy to be damaged. The shear force generated by rotation is much larger than the shear force in practical application. The durability of Al sheets coated with PTFE nanoparticles and infused with PFPE lubricant was investigated by the shear–spinning tests (Fig. 2(c)). Firstly, the lubricant-keeping capacity of SLIPSs was tested. Figures 2(d) and 2(e) showed the reserved mass of lubricant per unit area of FOP-*x* and FEP-*x* after undergoing the shear–spinning tests at the spin rate of 1,000–8,000 rpm for 10 s. The reserved mass of SLIPSs was decreased as the spin rate increasing, illustrating the more leaking lubricant mass as the greater shear force subjected to SLIPSs. Among the OP-*x* samples infused with PFPE, the sample of FOP-60 showed the best lubricant retention at different spin rate (Fig. 2(d)). The lubricant-keeping capacity was generally proportional to the concentrations of PTFE dispersion coated on the OP-*x* surfaces. The higher concentrations of PTFE dispersion, the better the lubricant-keeping capacity. On the surfaces of OP-*x*, the lubricant penetrates into the gaps of the PTFE nanoparticles. When subjected to shear force, the PTFE nanoparticle layer can retain the lubricant. When the concentration of PTFE dispersion was 10 wt%, PTFE nanoparticles did not completely cover the O-Al surfaces. Only a thin layer of PTFE nanoparticles could retain lubricant when subjected to shear force. With the increase of PTFE dispersion concentrations, the thickness of PTFE layer increases (Fig. S3 in the ESM), and the PTFE nanoparticles completely covered the O-Al surfaces. With the increased of PTFE layer thickness, the lubricant-keeping capacity was strengthened at the same shear rate. Meanwhile, the different concentrations of PTFE dispersion have no significant impact on the lubricant-keeping capacity of the FEP-*x* (Fig. 2(d)), which was mainly due to the step-like microstructure of EP-*x*. When the concentration of PTFE dispersion was lower than 20 wt%, the PTFE nanoparticles were sporadically distributed in the step-like structure of E-Al surfaces. The sporadically distributed PTFE nanoparticles basically had no effect on the roughness compared with the step-like microstructure. When subjected to shear force, the lubricant was strongly retained through permeating in the step-like structure with PTFE nanoparticles filled. With the concentrations of PTFE dispersion increasing, the PTFE nanoparticles

gradually filled the step-like structure of E-Al, and the lubricant penetrated into the PTFE nanoparticles on the step-like structure. When suffering the shear force, the lubricant was mainly retained in the stepped structure. That's the reason of the stable lubricant-keeping capacity of FEP-*x* under different concentrations of PTFE dispersion. Meanwhile, the lubricant-keeping capacity of SLIPSs with O-Al and E-Al as substrates was comparable under lower spin rates. However, as the spin coating rate increases, the lubricant-keeping capacity of SLIPSs with O-Al as substrates decreases faster than that of SLIPSs with E-Al as substrates, which was derived from the strengthen lubricant-keeping capacity of step-like microstructure of E-Al. These results demonstrated the structure was the mainly factors in the lubricant-keeping capacity.

Secondly, the durability of FOP-*x* and FEP-*x* was evaluated by exerting a high shear force (at spin rate of 8,000 rpm for 10 s). The CAs and SAs of FOP-*x*, FEP-*x*, 8000-FOP-*x*, and 8000-FEP-*x* were tested to measure the durability of the SLIPSs. After being infused the PFPE lubrication, the water CAs of FOP-*x* and FEP-*x* were barely fluctuated as the concentrations varies and stabled around 100° (Fig. 2(f)), which was due to the uniform PFPE lubricant layer on the PTFE nanoparticles coated O-Al and E-Al. Due to the low roughness, the water SAs of FOP-*x* also weren't fluctuated very much as the concentrations varies. Similarly, since the roughness of EP-*x* was decreased as the concentrations of PTFE dispersion increasing, the water SAs were also decreased (Fig. 2(g)). Although the excellent lubricant-keeping capacity of EP-*x*, the SAs of FOP-*x* were lower than that of FEP-*x*. The higher roughness was benefit to keep lubricant in the microstructure, but most of the lubricant were trapped in the step-like rough structure of E-Al, which was unhelpful to the water slide off the surfaces. And the micro-bulges in the rough structure also hindered the water slide off the surfaces.

After undergoing the high shear force, the CAs and SAs of 8000-FOP-*x* and 8000-FEP-*x* were investigated as shown in Figs. 2(h) and 2(i). The water CAs of 8000-FOP-*x* and 8000-FEP-*x* weren't fluctuated very much and stabled around 110° because of the stable PEPE lubricant layer. The water SAs of 8000-FOP-*x* were around 9°. Therein, the water SAs of 8000-FEP-45 and 8000-FEP-60 were around 14° and 57°, respectively. However, the droplets were pinned on the surfaces of 8000-FEP-10, 8000-FEP-20, and 8000-FEP-30. Figure S5 in the ESM show the roughness of 8000-FEP-*x*, which was similar with the roughness of EP-*x*. This confirmed that most of the lubricant was stocked into the step-like microstructure. In addition, the water can slide off the 8000-FEP-45 and 8000-FEP-60 with a higher inclination, but can slip off the 8000-FOP-*x* only with a small inclination. This reflected that the low roughness was beneficial to water sliding off the SLIPSs. The effective contact and separation of the water from the friction electrodes is necessary due to the horizontal vibration process of TENG, and a water film will be formed if small droplets adhered on the friction electrodes, which will hinder the effective contact and separation of water and friction electrodes, and reducing the TENG performance. Moreover, the velocity of droplets of different sizes sliding off the 8000-FOP-60 and 8000-FEP-60 with the fixed inclination of 25° was tested (Fig. S6 in the ESM). The velocity of different size droplets on the surface of 8000-FEP-60 was slower than that of the surface 8000-FOP-60, and 3 μL droplets still slid off the surface of 8000-FOP-60, which also demonstrated the excellent slippery properties of the FOP-*x*.

The output performances of hydrophobic/SLIPSs TENG based on different interfacial peculiarities were studied. As shown in Fig. 1(a), the hydrophobic TENG devices were assembled with two OP-*x* or EP-*x* as solid friction materials, deionized water as liquid friction material and PC tube as the water container. The SLIPSs TENG devices was assembled with two FOP-*x* or FEP-*x* as liquid friction materials, and deionized water as the other liquid friction materials and PC tube as the water container similarly. The frictional charges were generated between the friction pairs by periodicity horizontal mechanical vibration, and the mechanical energy was converted into electrical energy by this process. Figure 3 showed the working mechanism of the hydrophobic TENG. During the horizontal mechanical vibration of TENG system, the deionized water alternated contact and separation with the two sides substrates to enable the continuous contact and separation between the friction

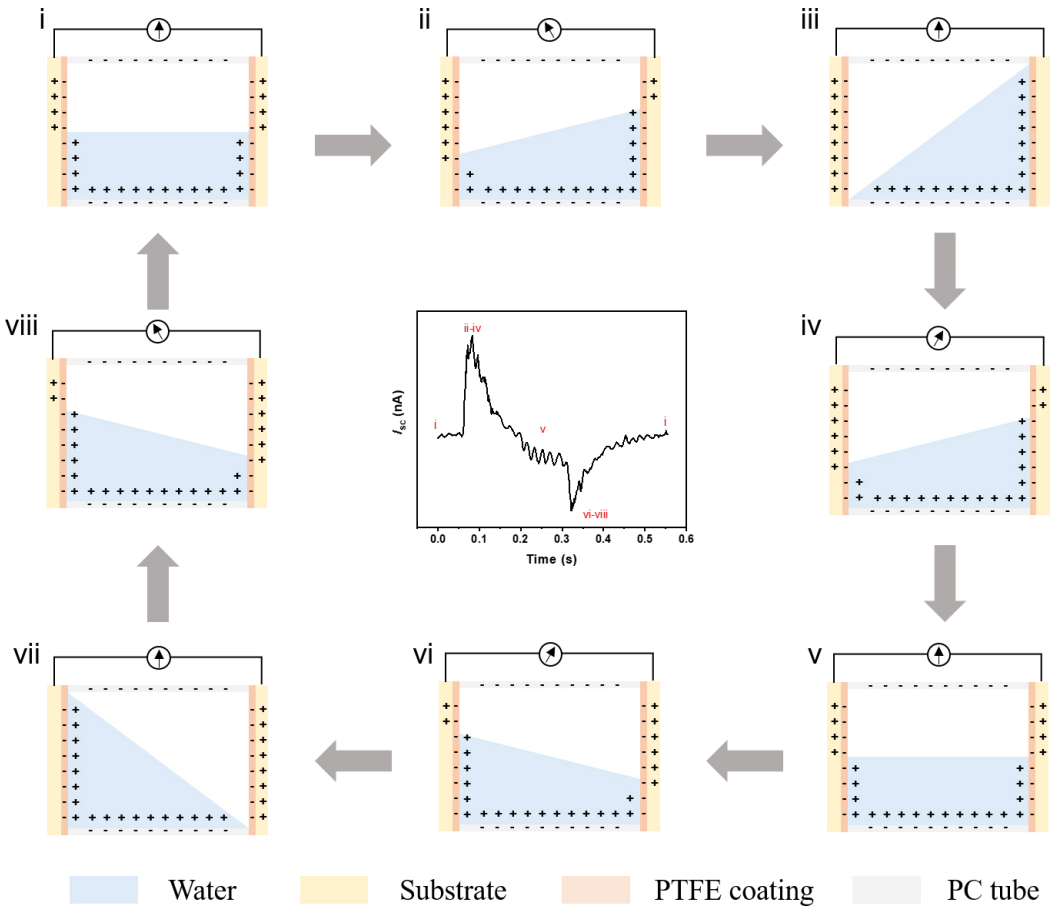

Fig. 3 Working mechanism of the hydrophobic TENG and the I_{sc} during one vibration cycle of OP-60. (i–iii) Asymmetric accumulation process of OP-60 TENG from the equilibrium state to the right maximum asymmetric accumulation state, corresponding to the positive increasing of I_{sc}. (iii–v) Asymmetric accumulation process of OP-60 TENG from the right maximum asymmetric accumulation state to the equilibrium state, corresponding to the positive decreasing of I_{sc}. (v–vii) Asymmetric accumulation process of OP-60 TENG from the equilibrium state to the left maximum asymmetric accumulation state, corresponding to the negative increasing of I_{sc}. (vii–i) Asymmetric accumulation process of OP-60 TENG from the left maximum asymmetric accumulation state to the equilibrium state, corresponding to the negative decreasing of I_{sc}.

pairs. Due to the fluidity of liquid, the closer contact between solid and liquid friction materials, the easier the electron transfer [17]. The contact and separation between water and the two sides of substrates produced potential difference during the TENG system horizontal vibration.

Firstly, this work explored the effects of substrate structure and concentrations of PTFE dispersion on the output performances of hydrophobic TENG devices. The hydrophobic TENG devices assembled by OP-*x* and EP-*x* as solid fiction materials were marked as OP-*x* TENG and EP-*x* TENG, respectively. Figures 4(a)–4(d) and S7 in the ESM show the output performances of the hydrophobic TENG devices. Therein, the data of the I_{sc} and V_{oc} of EP-10, EP-20, EP-30, and EP-45, the V_{oc} of EP-60, the I_{sc} of OP-10, OP-20, and OP-30 were smoothed for convenient analyzing. The I_{sc} and V_{oc} were increased as the PTFE dispersion concentrations increasing, whether the solid friction materials were based on the O-Al or E-Al. The output performances of hydrophobic TENG devices were greatly improved when the PTFE dispersion concentrations was greater than 20 wt%. And output performances of the OP-*x* TENG were superior than that of EP-*x* TENG at all the PTFE dispersion concentrations. This was because the O-Al surfaces can accommodate more PTFE nanoparticles than that of E-Al, resulting in a larger charge density. The electron transfer plays a dominant role in this hydrophobic-water interfacial triboelectrification

situation since the deionized water was employed as liquid materials [41, 42]. Next, because of the fluidity, water molecules were easily permeated into the space between the PTFE nanoparticles and contact with the surface of the hydrophilic Al sheets when the surfaces water adhesion force was larger. The strong water adhesion force on the surfaces of EP-10 and EP-20 resulting the water pinned on the electrodes, inhibiting the transfer of friction charges. Although the smallest surface adhesion of EP-45 made separation of the water from the PTFE layer easier, the more PTFE nanoparticles on the surface of EP-60 can produce more friction charges, and thus the sample EP-60 show superior output performances than that of EP-45. With the increasing of PTFE dispersion concentrations, the surfaces show higher hydrophobic. Compared with EP-45, it is more difficult for water molecules to penetrate into the space of PTFE nanoparticles on the surface of EP-60, and contact the hydrophilic Al sheet. The contact and separation of water and PTFE coated Al sheets were easier as the PTFE dispersion concentrations increasing, and the charges transferred barely without barriers. However, the PTFE nanoparticles gradually filled in the step-like microstructure of E-Al surfaces as the increase of PTFE dispersion concentrations, bits of hydroxyl-rich bulges still exposed on the EP-60, resulting in the inferior output performances than that of OP-60. The more PTFE nanoparticles on the OP-x surfaces than EP-x resulting in the superior output performances of OP-x TENG than that of the EP-x TENG.

Despite the excellent hydrophobic of PTFE layer, the trapped air between the PTFE nanoparticles can be easily depleted in high humidity conditions, resulting in the droplets pinned on the hydrophobic surfaces and decreasing the output performance of hydrophobic TENG. Beyond that, the SLIPSs are a proper alternative due to the superior characteristics in stability and durability. Thus, the studies of SLIPSs TENG have profound significance for improving the durability of TENG. The SLIPSs TENG devices were assembled by the SLIPSs of FOP-60 as the liquid friction materials, and water as another liquid friction materials. The effects of PFPE thickness on the output performances of the SLIPSs TENG devices were researched as shown in Figs. 4(e), 4(f), and S9 in the ESM. The PFPE thickness of FOP-60 was controlled by applying the certain spin rate. Figure S8 in the ESM show the PFPE thickness of FOP-60 after undergoing the spin rate of 1,000–8,000 rpm for 10 s. The SLIPSs of 1000-FOP-60 and 2000-FOP-60 can't be

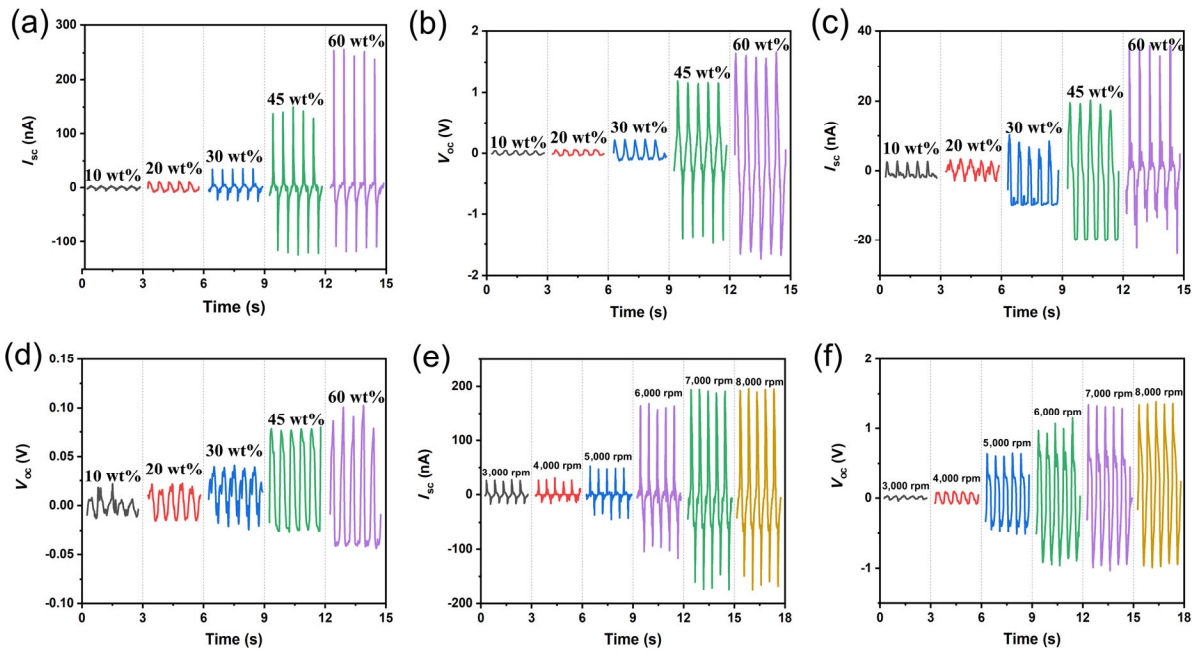

Fig. 4 Effects of substrate structure, concentrations of PTFE dispersion, and PFPE thickness on the output performances of the hydrophobic TENG and SLIPSs TENG devices. (a) I_{sc} and (b) V_{oc} of the OP-x TENG, (c) I_{sc} and (d) V_{oc} of the EP-x TENG with different concentrations PTFE dispersion. (e) I_{sc} and (f) V_{oc} of the y-FOP-60 SLIPSs TENG with different spin rate.

assembled as SLIPSs TENG due to the thicker PFPE layer. The PFPE thickness of 3000-FOP-60 was about 11.36 μm, which was about 3 times of 8000-FOP-60 (4.07 μm). The I_{sc} and V_{oc} of SLIPSs TENG were increasing as the thinning PFPE layer, and was stable after 6,000 rpm. The output performances of 7000-FOP-60 and 8000-FOP-60 TENG were just below than OP-60 TENG. When the oil layer was thicker, the PFPE layer covered the PTFE layer, and the water mainly contacted and separated with PFPE layer during the horizontal vibrations. When sliding off the thinner PFPE coated substrates, the droplets will contact the PTFE layer more than the lubricant layer. According to the recent research, the friction charges generated by the water and PFPE, PFPE and PTFE layer interface are insignificant and can be ignored compared to that on the water and SLIPSs interfaces, the PFPE layer had charge transparency behavior in the triboelectrification of single-electrode mode SLIPSs TENG [44]. Due to the negligible friction charges generated by the water and PFPE, PFPE and PTFE layer interface, the output performances of the OP-60 TENG and 8000-FOP-60 SLIPSs TENG were mainly affected by the PFPE thickness.

To further study the triboelectrification behavior of the OP-60 TENG and 8000-FOP-60 SLIPSs TENG devices, the performances of ethylene glycol-based TENG and the response of OP-60 TENG, 8000-FOP-60 SLIPSs TENG to different NaCl ionic concentrations were investigated. In order to easily distinguish, the water-based and ethylene glycol-based OP-60 TENG were marked as W-OP-60 TENG and EG-OP-60 TENG, and the water-based and ethylene glycol-based 8000-FOP-60 SLIPSs TENG were marked as W-8000-FOP-60 SLIPSs TENG and EG-8000-FOP-60 SLIPSs TENG, respectively. Figure 5(a) showed the output performances of W-OP-60 TENG and W-8000-FOP-60 SLIPSs TENG which were still slightly lower than that of W-OP-60 TENG since the thin PFPE layer still exist. Figures 5(b) and 5(c) showed the I_{sc} comparisons of W-OP-60 vs. EG-OP-60 TENG and W-8000-FOP-60 vs. EG-8000-FOP-60 SLIPSs TENG. The similar values of the I_{sc} further proved that the triboelectrification of OP-60 TENG and 8000-FOP-60 SLIPSs TENG were dominated by electron transfer rather than ion transfer since ethylene glycol is non-electrolyte and polar

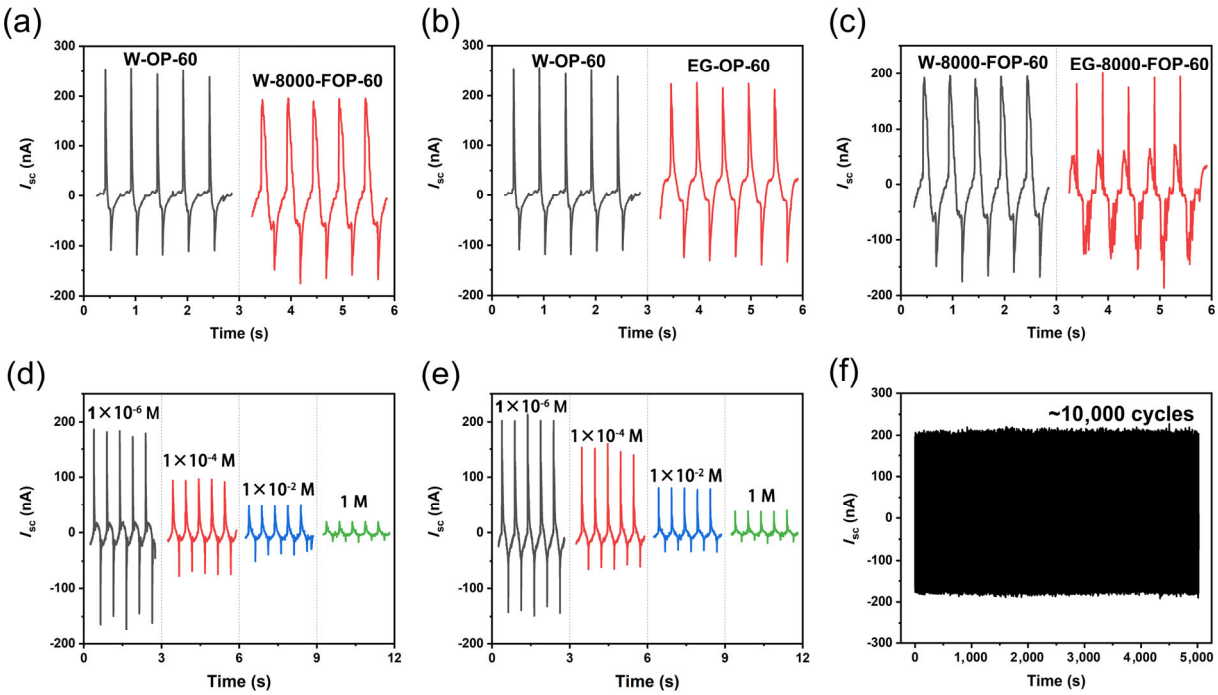

Fig. 5 Triboelectrification behavior of the OP-60 TENG and 8000-FOP-60 SLIPSs TENG. (a) I_{sc} of W-OP-60 TENG and W-8000-FOP-60 SLIPSs TENG. (b) I_{sc} comparisons of the W-OP-60 TENG vs. EG-OP-60 TENG, and (c) the W-8000-FOP-60 SLIPSs TENG vs. EG-8000-FOP-60 SLIPSs TENG. Response of (d) OP-60 TENG and (e) 8000-FOP-60 SLIPSs TENG to NaCl concentrations from 10^{-6} to 1 M. (f) Stability test of the W-8000-FOP-60 TENG over about 10,000 cycles.

molecule [44]. Figures 5(d) and 5(e) showed the OP-60 TENG and 8000-FOP-60 SLIPSs TENG response to the NaCl concentrations. If there is ion transfer in the tribally charged pair, with the increase of ion concentration, the electron transfer will first enhance and then weaken, and the I_{sc} will first increase and then decrease. When there is no electron transfer, the higher ion concentration will inhibit the electron transfer at the interface, and the I_{sc} will decrease with the increase of ion concentration in the solution [19]. Conversely, the output performances of the OP-60 TENG and 8000-FOP-60 SLIPSs TENG were decreasing as the ionic concentrations increasing. Thus, it can be considered that the triboelectrification of the OP-60 TENG and 8000-FOP-60 SLIPSs TENG was also dominated by electron transfer [44]. The stability test of the 8000-FOP-60 TENG over about 10,000 cycles was investigated as shown in Fig. 5(f), which exhibited the excellent stability of the SLIPSs TENG.

By means of superior stability and durability of SLIPSs, SLIPSs TENG also exhibited a strong stability under the harsh surroundings, such as different temperature, high humidity, and being destroyed by scratches. Due to the generally low temperature and high humidity of ocean surface, the effect of low temperature and high humidity on the performance of SLIPSs TENG needs to be studied. The low temperature and high humidity stability tests of the hydrophobic and SLIPSs TENG devices were shown in Figs. 6(a)–6(d) and 6(e)–6(h). The output performances of the OP-60 TENG were susceptible by the low temperature and high humidity. Nevertheless,

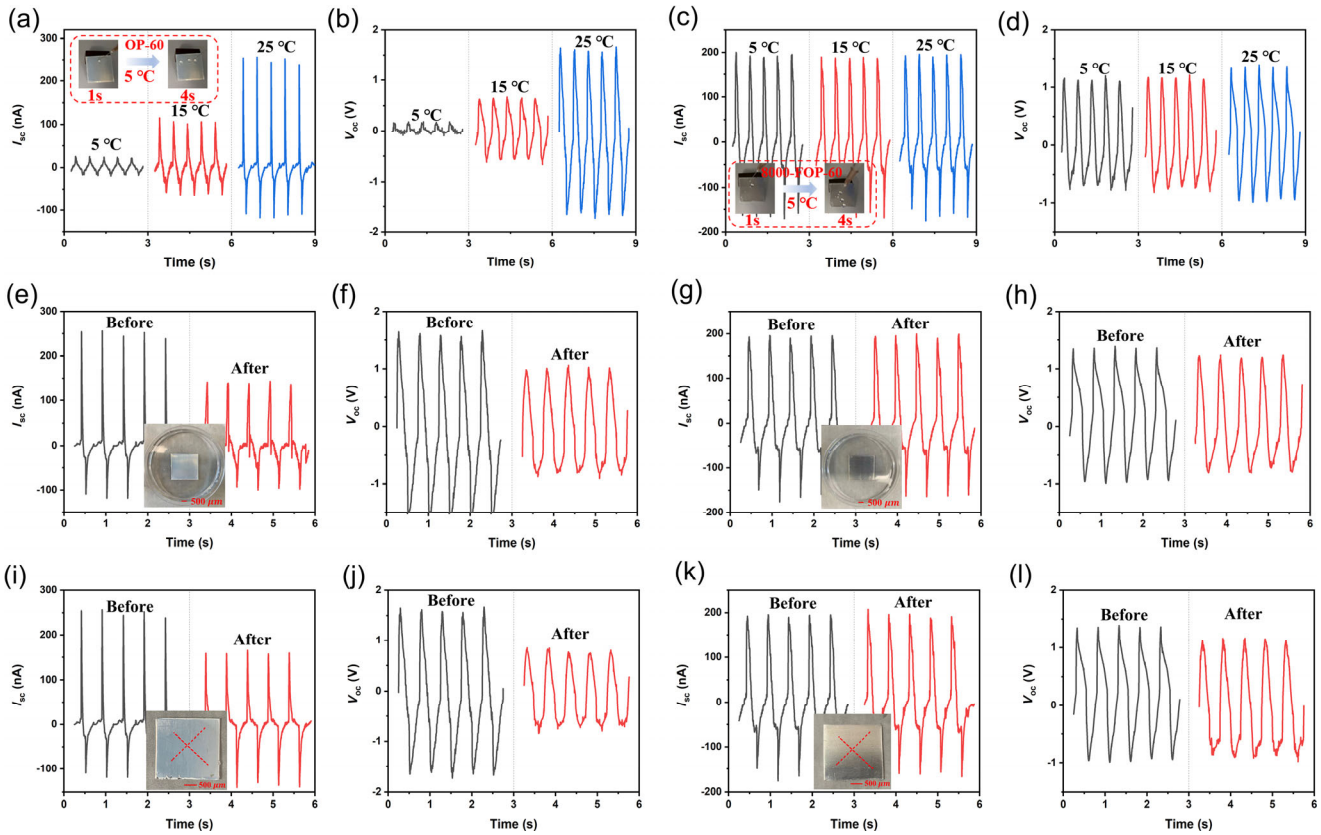

Fig. 6 Stability and durability tests of the hydrophobic/SLIPSs TENG devices. (a) I_{sc} and (b) V_{oc} of the OP-60 TENG at different temperature, (c) I_{sc} and (d) V_{oc} of the 8000-FOP-60 SLIPSs TENG at different temperature, the insets in (a) and (c) were the sliding process of droplets on the surfaces of OP-60 and 8000-FOP-60 at about 5 °C with inclination angle of 30°, respectively. (e) I_{sc} and (f) V_{oc} of the OP-60 TENG before and after being immersed in water for 48 h, (g) I_{sc} and (h) V_{oc} of the 8000-FOP-60 TENG before and after being immersed in water for 48 h, the insets in (e) and (g) were the images of the samples of OP-60 and 8000-FOP-60 that be immersed in water, respectively. (i) I_{sc} and (j) V_{oc} of the OP-60 TENG before and after the surfaces were destroyed by scratches, (k) I_{sc} and (l) V_{oc} of the 8000-FOP-60 SLIPSs TENG before and after the surfaces were destroyed by scratches, the insets in (i) and (k) were the images of the surfaces of OP-60 and 8000-FOP-60 were destroyed by scratches, respectively.

the SLIPSs TENG were generally not affected by the low temperature and high humidity. The enhanced stabilities of 8000-FOP-60 TENG than OP-60 TENG at low temperature and high humidity conditions were attributed to that the homogeneous and stable solid–liquid interface of the SLIPSs had no adsorption sites for droplets, and guaranteed the effective separation of water from the electrodes under low temperature and high humidity, making the efficient electron transfer. For further verifying this standpoint, the sliding process of droplets on the surfaces of OP-60 and 8000-FOP-60 at 5 °C was observed as shown in the inset of Figs. 6(a), 6(c), and S10 in the ESM. At the condition of 5 °C, the droplet slid off the 8000-FOP-60 but pinned on the OP-60. Thanks to the PFPE layer on the substrates, the contact and separation of water and substrates were insusceptible in harsh environments, ensuring the stable output of SLIPSs TENG. Figures 6(i)–6(l) showed the durability tests by creating surface scratches on the substrates. Similarly, the output performances of OP-60 TENG were more susceptible than that of 8000-FOP-60 SLIPSs TENG, which also demonstrated the PFPE layer was beneficial to a stable output performance of SLIPSs TENG. For further verifying the superior stability and durability of SLIPSs TENG, the light emitting diode (LED, 2.2 V, 0.2 μA) was lit by the integrated circuit which was powered by the two same TENG devices and rectified by a rectifier bridge (Fig. 7(a)). Figures 7(b)–7(e) showed the LED lighting status at 5 and 20 °C of the OP-60 TENG Figs. 7(b) and 7(d) 8000-FOP-60 SLIPSs TENG (Figs. 7(c) and 7(e)). The OP-60 TENG was fails to function, but the 8000-FOP-60 SLIPSs TENG still function at low temperature. Hence, the introduce of SLIPSs in TENG did improve the stability and durability.

4 Conclusions

In summary, the triboelectrification at the hydrophobic/slippery substrate–water interfaces were explored based on the different interfacial characteristics. Firstly, polytetrafluoroethylene (PTFE) nanoparticles were coated on Al sheets with different structures by a simple spin-coating method. Compared with the substrates of E-Al with microstructure, the substrate of O-Al with flat structure can accommodate more PTFE nanoparticles. Although the lubricant-keeping capacity of OP were not as good as that of EP with step-like microstructure, the OP exhibited superior slippery performances than that of EP after undergoing high shear force due to its lower roughness. The contact triboelectrification performances were investigated based on the different PTFE dispersion concentrations coated O-Al and E-Al. The results manifested the triboelectrification performances of OP-TENG was better than that of EP-TENG duo to the more PTFE nanoparticles. Furthermore, the slippery surfaces–water triboelectrification performances were investigated

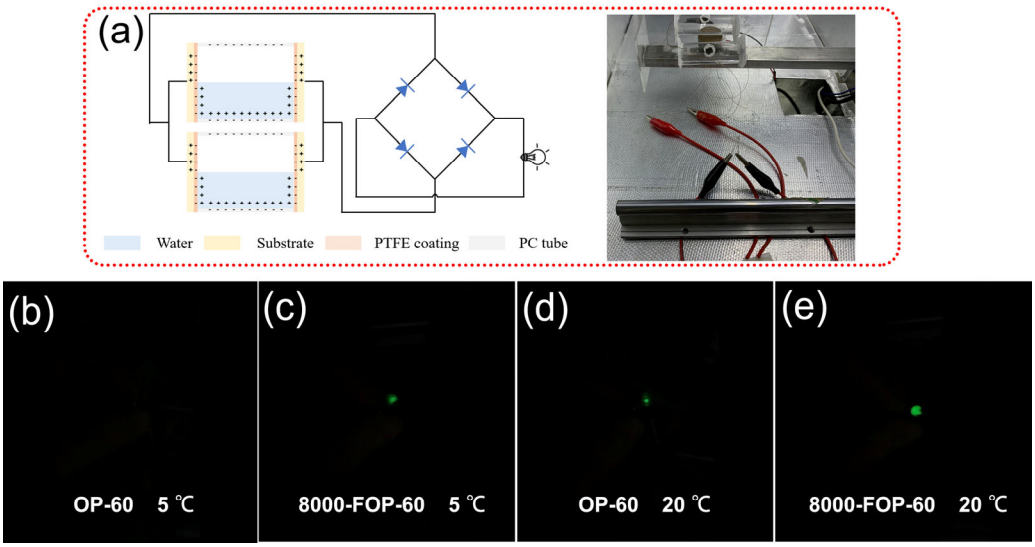

Fig. 7 (a) Schematics and photographs of the integrated circuit to lit the LED (2.2 V, 0.2 μA). Photographs of the lighting LED demonstration (b, c) at 5 °C of OP-60 TENG and 8000-FOP-60 SLIPSs TENG, and (d, e) at 20 °C of OP-60 TENG and 8000-FOP-60 SLIPSs TENG.

based on perfluoropolyether (PFPE) infused OP-60 surfaces. The PTFE thickness was one of the key factors on the triboelectrification. With the decreasing of PFPE thickness, the contact probability between water and PTFE layer increases, and the triboelectrification performance improves. Both the triboelectrification behavior of hydrophobic/slippery substrate surfaces–water TENG assembled in this work were dominated by the electron transfer. Thanks to the introduction of slippery lubricant-infused surfaces (SLIPSs), the SLIPSs TENG maintained excellent triboelectrification performances and showed excellent stability and durability when suffering from harsh environments.

Acknowledgements

This work was financially supported by the National Natural Science Foundation of China (Nos. 51735013 and 51905520).

Electronic Supplementary Material: Supplementary material is available in the online version of this article at https://doi.org/10.1007/s40544-022-0646-1.

References

[1] Tabor D P, Roch L M, Saikin S K, Kreisbeck C, Sheberla D, Montoya J H, Dwaraknath S, Aykol M, Ortiz C, Tribukait H, Amador–Bedolla C, Brabec C J, Maruyama B, Persson K A, Aspuru–Guzik A. Accelerating the discovery of materials for clean energy in the era of smart automation. *Nat Rev Mater* **3**(5): 5–20 (2018)

[2] Park S, Heo S W, Lee W, Inoue D, Jiang Z, Yu K, Jinno H, Hashizume D, Sekino M, Yokota T, Fukuda K, Tajima K, Someya T. Self-powered ultra-flexible electronics via nano-grating-patterned organic photovoltaics. *Nature* **561**(7724): 516–521 (2018)

[3] Yin X X, Zhao X W, Zhang W C. A novel hydro-kite like energy converter for harnessing both ocean wave and current energy. *Energy* **158**: 1204–1212 (2018)

[4] Melo A B, Sweeney E, Luis Vitiate J. Global review of recent ocean energy activities. *Mar Technol Soc J* **47**(5): 97–103 (2013)

[5] Zhao X J, Kuang S Y, Wang Z L, Zhu G. Highly adaptive solid-liquid interfacing triboelectric nanogenerator for harvesting diverse water wave energy. *ACS Nano* **12**(5): 4280–4285 (2018)

[6] Zhang Z H, Li X M, Yin J, Xu Y, Fei W W, Xue M M, Wang Q, Zhou J X, Guo W L. Emerging hydrovoltaic technology. *Nat Nanotechnol* **13**(12): 1109–1119 (2018)

[7] Wang J, Wu C S, Dai Y J, Zhao Z H, Wang A, Zhang T J, Wang Z L. Achieving ultrahigh triboelectric charge density for efficient energy harvesting. *Nat Commun* **8**: 88 (2017)

[8] Sun W, Zheng Y, Li T, Feng M, Cui S, Liu Y, Chen S, Wang D. Liquid-solid triboelectric nanogenerators array and its applications for wave energy harvesting and self-powered cathodic protection. *Energy* **217**:119388 (2021)

[9] Sun L, Chen S, Guo Y, Song J, Zhang L, Xiao L, Guan Q, You Z. Ionogel-based, highly stretchable, transparent, durable triboelectric nanogenerators for energy harvesting and motion sensing over a wide temperature range. *Nano Energy* **63**: 103847 (2019)

[10] Wang X, Niu S, Yin Y, Yi F, You Z, Wang Z L. Triboelectric nanogenerator based on fully enclosed rolling spherical structure for harvesting low-frequency water wave energy. *Adv Energy Mater* **5**(24): 1501467 (2015)

[11] Li X, Zhang L, Feng Y, Zhang X, Wang D, Zhou F. Solid-liquid triboelectrification control and antistatic materials design based on interface wettability control. *Adv Funct Mater* **29**(35): 1903587 (2019)

[12] Jurado U T, Pu S H, White N M. Wave impact energy harvesting through water-dielectric triboelectrification with single-electrode triboelectric nanogenerators for battery-less systems. *Nano Energy* **78**: 105204 (2020)

[13] Wei X, Zhao Z, Zhang C, Yuan W, Wu Z, Wang J, Wang Z L. All-weather droplet-based triboelectric nanogenerator for wave energy harvesting. *ACS Nano* **15**: 13200–13208 (2021)

[14] Xu C G, Liu Y, Liu Y P, Zheng Y B, Feng Y G, Wang B Q, Kong X, Zhang X L, Wang D A. New inorganic coating-based triboelectric nanogenerators with anti-wear and self-healing properties for efficient wave energy harvesting. *Appl Mater Today* **20**: 100645 (2020)

[15] Wang Y, Gao S W, Xu W H, Wang Z K. Nanogenerators with superwetting surfaces for harvesting water/liquid energy. *Adv Funct Mater* **30**(26): 1908252 (2020)

[16] Shi Q F, Wang H, Wu H, Lee C K. Self-powered triboelectric nanogenerator buoy ball for applications ranging from environment monitoring to water wave energy farm. *Nano Energy* **40**: 203–213 (2017)

[17] Wang Z L, Wang AC. On the origin of contact-electrification. *Materials Today* **30**: 34–51 (2019)

[18] Nie J, Ren Z, Xu L, Lin S, Zhan F, Chen X, Wang Z L. Probing contact-electrification-induced electron and ion transfers at a liquid-solid interface. *Adv Mater* **32**(2): 1905696 (2020)

[19] Zhang L, Li X, Zhang Y, Feng Y, Zhou F, Wang D. Regulation and influence factors of triboelectricity at the solid-liquid interface. *Nano Energy* **78** :105380 (2020)

[20] Wang K, Li J. Electricity generation from the interaction of liquid-solid interface: A review. *J Mater Chem A* **9**(14): 8870–8895 (2021)

[21] Lin S Q, Xu L, Wang A C, Wang Z L. Quantifying electron-transfer in liquid-solid contact electrification and the formation of electric double-layer. *Nat Commun* **11**(1): 399 (2020)

[22] Yang Y, Zhang H, Chen J, Jing Q, Zhou Y S, Wen X, Wang Z L. Single-electrode-based sliding triboelectric nanogenerator for self-powered displacement vector sensor system. *ACS Nano* **7**(8): 7342–7351 (2013)

[23] Ravelo B, Duval F, Kane S, Nsom B. Demonstration of the triboelectricity effect by the flow of liquid water in the insulating pipe. *J Electrostat* **69**(6): 473–478 (2011)

[24] Lee J–W, Hwang W. Theoretical study of micro/nano roughness effect on water-solid triboelectrification with experimental approach. *Nano Energy* **52**: 315–322 (2018)

[25] Chen J, Guo H, Zheng J, Huang Y, Liu G, Hu C, Wang Z L. Self-powered triboelectric micro L liquid/gas flow sensor for microfluidics. *ACS Nano* **10**(8): 8104–8112 (2016)

[26] Tang Q, Zhang H, He B, Yang P. An all-weather solar cell that can harvest energy from sunlight and rain. *Nano Energy* **30**: 818–824 (2016)

[27] Jiang P, Zhang L, Guo H, Chen C, Wu C, Zhang S, Wang Z L. Signal output of triboelectric nanogenerator at oil-water-solid multiphase interfaces and its application for dual-signal chemical sensing. *Adv Mater* **31**(39): 1902793 (2019)

[28] Lin Z–H, Cheng G, Lee S, Pradel K C, Wang Z L. Harvesting water drop energy by a sequential contact-electrification and electrostatic-induction process. *Adv Mater* **26**(27): 4690–4696 (2014)

[29] Li X, Zhang L, Feng Y, Zheng Y, Wu Z, Zhang X, Wang N, Wang D, Zhou F. Reversible temperature-sensitive liquid-solid triboelectrification with polycaprolactone material for wetting monitoring and temperature sensing. *Adv Funct Mater* **31**(17): 2010220 (2021)

[30] Wong T S, Kang S H, Tang S K Y, Smythe E J, Hatton B D, Grinthal A, Aizenberg J. Bioinspired self-repairing slippery surfaces with pressure-stable omniphobicity. *Nature* **477**(7365): 443–447 (2011)

[31] Han X, Tang X, Chen R, Li W, Zhu P, Wang L. Citrus-peel-like durable slippery surfaces. *Chem Eng J* **420**: 129599 (2021)

[32] Yu M N, Liu M M, Zhang D D, Fu S H. Lubricant-grafted omniphobic surfaces with anti-biofouling and drag-reduction performances constructed by reactive organic-inorganic hybrid microspheres. *Chem Eng J* **422**: 130113 (2021)

[33] Li R, Zhao L, Yao A, Si D, Shang Y, Ding X, An H, Ye H, Zhang Y, Li H. Design of lubricant-infused surfaces based on mussel-inspired nanosilica coatings: Solving adhesion by pre-adhesion. *Langmuir* **37**: 10708–10719 (2021)

[34] Kim P, Wong T S, Alvarenga J, Kreder M J, Adorno–Martinez W E, Aizenberg J. Liquid-infused nanostructured surfaces with extreme anti-ice and anti-frost performance. *ACS Nano* **6**(8): 6569–6577 (2012)

[35] Chen Y, Guo Z. An ionic liquid-infused slippery surface for temperature stability, shear resistance and corrosion resistance. *J Mater Chem A* **8**(45): 24075–24085 (2020)

[36] Howell C, Grinthal A, Sunny S, Aizenberg M, Aizenberg J. Designing liquid-infused surfaces for medical applications: A review. *Adv Mater* **30**(50): 1802724 (2018)

[37] Chen X, Wen G, Guo Z. What are the design principles, from the choice of lubricants and structures to the preparation method, for a stable slippery lubricant-infused porous surface? *Mater Horiz* **7**: 1697–1726 (2020)

[38] Rykaczewski K, Anand S, Subramanyam S B, Varanasi K K. Mechanism of frost formation on lubricant-impregnated surfaces. *Langmuir* **29**(17): 5230–5238 (2013)

[39] Baumli P, D'Acunzi M, Hegner K I, Naga A, Wong W S Y, Butt H-J, Vollmer D. The challenge of lubricant-replenishment on lubricant-impregnated surfaces. *Adv Colloid Interfac* **287**: 102329 (2021)

[40] Lin S Q, Chen X Y, Wang Z L. Contact electrification at the liquid–solid interface. *Chem Rev* **122**(5): 5209–5232 (2022)

[41] Lin S Q, Xu L, Zhu L P, Chen X Y, Wang Z L. Electron transfer in nanoscale contact electrification: Photon excitation effect. *Adv Mater* **31**(27): 1901418 (2019)

[42] Li S Y, Nie J H, Shi Y X, Tao X L, Wang F, Tian J W,

Lin S Q, Chen X Y, Wang Z L. Contributions of different functional groups to contact electrification of polymers. *Adv Mater* **32**(25): 2001307 (2020)

[43] Xu W H, Zhou X F, Hao C L, Zheng H X, Liu Y, Yan X T, Yang Z B, Leung M, Zeng X C, Xu R X, Wang Z K. Slips-TENG: Robust triboelectric nanogenerator with optical and charge transparency using a slippery interface. *Natl Sci Rev* **6**(3): 540–550 (2019)

[44] Lin S, Zheng M, Luo J, Wang Z L. Effects of surface functional groups on electron transfer at liquid-solid interfacial contact electrification. *ACS Nano* **14**(8): 10733–10741 (2020)

[45] Cao S, Zhang H, Cui X, Yuan Z, Ding J, Sang S. Fully-enclosed metal electrode-free triboelectric nanogenerator for scavenging vibrational energy and alternatively powering personal electronics. *Adv Eng Mater* **21**(2): 1800823 (2019)

Yi CHEN. She is a Ph.D. candidate at Lanzhou Institute of Chemical Physics (LICP), Chinese Academy of Sciences (CAS) under the supervision of Prof. Zhiguang GUO. She received her B.S. degree (2016) and M.S. degree (2019) in North University of China (NUC) under the supervision of Prof. Chenyang XUE. Her current scientific interests are focused on liquid-infused surfaces and its application.

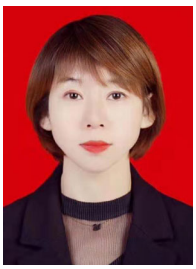

Jinxia HUANG. She received her Ph.D. degree from LICP, CAS in 2015. Then she joined Prof. GUO's biomimetic materials of tribology (BMT) group in LICP. Her current scientific interests are focused on the biomimetic materials of tribology and its application.

Zhiguang GUO. He received his Ph.D. degree from LICP, CAS in 2007. Then he joined Hubei University. From Oct 2007 to Aug 2008, he worked in University of Namur (FUNDP), Belgium, as a post-doctor. From Sep 2008 to Mar 2011, he worked in Funds of National Research Science (FNRS), Belgium, as a "charge de researcher". During Feb 2009 to Feb 2010, he worked in Department of Physics, University of Oxford, UK, as a visiting scholar. Now he is a full professor and the dean of School of Materials Science and Engineering, Hubei University. His current scientific interests are focused on the biomimetic materials of tribology and its application.

Weimin LIU. He received his Ph.D. degree in lubricating materials and tribology from LICP of CAS in 1990. Then he joined the State Key Laboratory of Solid Lubrication (LSL) of the LICP. From June 1993 to June 1994, he worked as a visiting scholar at Pennsylvania State University, USA. In 2013 and 2016, he was elected the Member of the Chinese Academy of Sciences and Fellow of The World Academy of Sciences (TWAS), respectively. Currently, he is a professor of LICP and head of the State Key Laboratory of Solid Lubrication. His research interests mainly focus on space and aviation lubrication, high performance lubricating materials, and Tribochemistry.